nature nanotechnology

ARTICLES

PUBLISHED ONLINE: 10 NOVEMBER 2014 | DOI: 10.1038/NNANO.2014.247

An all-in-one nanopore battery array

Chanyuan Liu[1,2], Eleanor I. Gillette[3†], Xinyi Chen[1,2,4†], Alexander J. Pearse[1,2], Alexander C. Kozen[1,2], Marshall A. Schroeder[1,2], Keith E. Gregorczyk[1,2,5], Sang Bok Lee[1,3*] and Gary W. Rubloff[1,2*]

A single nanopore structure that embeds all components of an electrochemical storage device could bring about the ultimate miniaturization in energy storage. Self-alignment of electrodes within each nanopore may enable closer and more controlled spacing between electrodes than in state-of-art batteries. Such an 'all-in-one' nanopore battery array would also present an alternative to interdigitated electrode structures that employ complex three-dimensional geometries with greater spatial heterogeneity. Here, we report a battery composed of an array of nanobatteries connected in parallel, each composed of an anode, a cathode and a liquid electrolyte confined within the nanopores of anodic aluminium oxide, as an all-in-one nanosize device. Each nanoelectrode includes an outer Ru nanotube current collector and an inner nanotube of V_2O_5 storage material, forming a symmetric full nanopore storage cell with anode and cathode separated by an electrolyte region. The V_2O_5 is prelithiated at one end to serve as the anode, with pristine V_2O_5 at the other end serving as the cathode, forming a battery that is asymmetrically cycled between 0.2 V and 1.8 V. The capacity retention of this full cell (relative to 1 C values) is 95% at 5 C and 46% at 150 C, with a 1,000-cycle life. From a fundamental point of view, our all-in-one nanopore battery array unveils an electrochemical regime in which ion insertion and surface charge mechanisms for energy storage become indistinguishable, and offers a testbed for studying ion transport limits in dense nanostructured electrode arrays.

Nanostructured electrodes hold great promise for future electrical energy storage devices, with their large surface areas and short ion transport time through the electrode enabling high energy storage at any given power density, and their enhanced mechanical properties under strain facilitating the fabrication of flexible architectures. Moreover, power and energy metrics could be further improved if anode and cathode nanostructures were to be brought into close proximity in a full cell configuration. Rolison and colleagues[1] have reported a random network architecture based on nanoporous, interconnected scaffolds on which conformal layers of anodic, electrolyte and cathodic materials are sequentially deposited to form a battery. Meanwhile, interdigitated three-dimensional architectures should allow denser packing of active storage electrodes at the micro- or nanoscale[2], but only a limited number of these regular three-dimensional micro- or nanoscale batteries have been fabricated that are able to operate successfully[3–5].

A fully interdigitated three-dimensional electrostatic nanocapacitor has been reported by Banerjee and co-authors[6], who used an ultrathin (~6 nm thick) dielectric to separate two electrodes self-aligned within an anodic aluminium oxide (AAO) nanopore. This nanodevice demonstrated a record areal capacity, with an estimated higher power density and increased energy density comparable to the low range values of electrochemical capacitors. Despite further performance improvements via nanoengineering[7], the intrinsically high leakage current of such ultrathin dielectrics limits charge retention and requires hybrid electrochemical–electrostatic circuits to retain the benefits of the three-dimensional nanoarchitecture device[8]. Replacing the dielectric with a solid-state electrolyte, in principle, gives a high-performance electrochemical storage device, but low ionic conductivity, interface defects and fabrication challenges pose serious challenges to this route towards a full storage device based on three-dimensional parallel nanostructures[2,9–11].

An alternative solution would be to use liquid organic electrolytes. An example of this configuration has been reported by Ajayan and co-authors[5], in which AAO nanopores were used to self-align nanowires of Ni–Sn (anode) and polyaniline (PANI) (cathode) immersed in a liquid electrolyte. However, the full cell device had a relatively low areal capacity (8–10 μAh cm^{-2}) compared to other self-assembled nanoarchitectures for energy storage[12,13]. The relatively low capacity of this full cell, especially when compared to the performance of the half-cell configuration, has raised questions about the practicability of head-to-head nanowire electrodes separated by an ultrathin electrolyte layer. A key concern relates to the low electronic and ionic conductivities within these high-aspect-ratio structures. It is possible that a significant number of Li ions are depleted in the nanoconfined environment near the electrode, because Li ions that are quickly transported through the solid electrolyte interface (SEI), especially when the device operates at high power, may not be replenished by Li ions from the bulk electrolyte reservoir. In addition, Li ion deficiency may also alter SEI formation and stability; higher than normal localized ion currents can be expected in this regime, as probed by scanning tunnelling microscopy (STM) and modelled theoretically[14,15]. A second concern arises from the electrode morphology. Complex three-dimensional structures may produce inhomogeneous electric fields and ionic concentration gradients, resulting in high local current densities that may cause undesired reactions at the SEI and generate leakage currents. In addition, thermal inhomogeneity may lead to device failure[16].

However, highly confined electrolyte environments are unavoidable if electrodes are densely arranged to take advantage of nanostructuring for high-power-storage applications. (Indeed, the tradeoff between using a nanostructured electrode and designing dense architectures may give rise to new scientific questions at the mesoscale[17].)

[1]Department of Materials Science and Engineering, University of Maryland, College Park, Maryland 20742, USA, [2]Institute for Systems Research, University of Maryland, College Park, Maryland 20742, USA, [3]Department of Chemistry and Biochemistry, University of Maryland, College Park, Maryland 20742, USA, [4]Lam Research Corporation, Tualatin, Oregon 97062, USA, [5]CIC nanoGUNE, 20012 Donostia, Gipuzkoa, Spain; †These authors contributed equally to this work. *e-mail: slee@umd.edu; rubloff@umd.edu

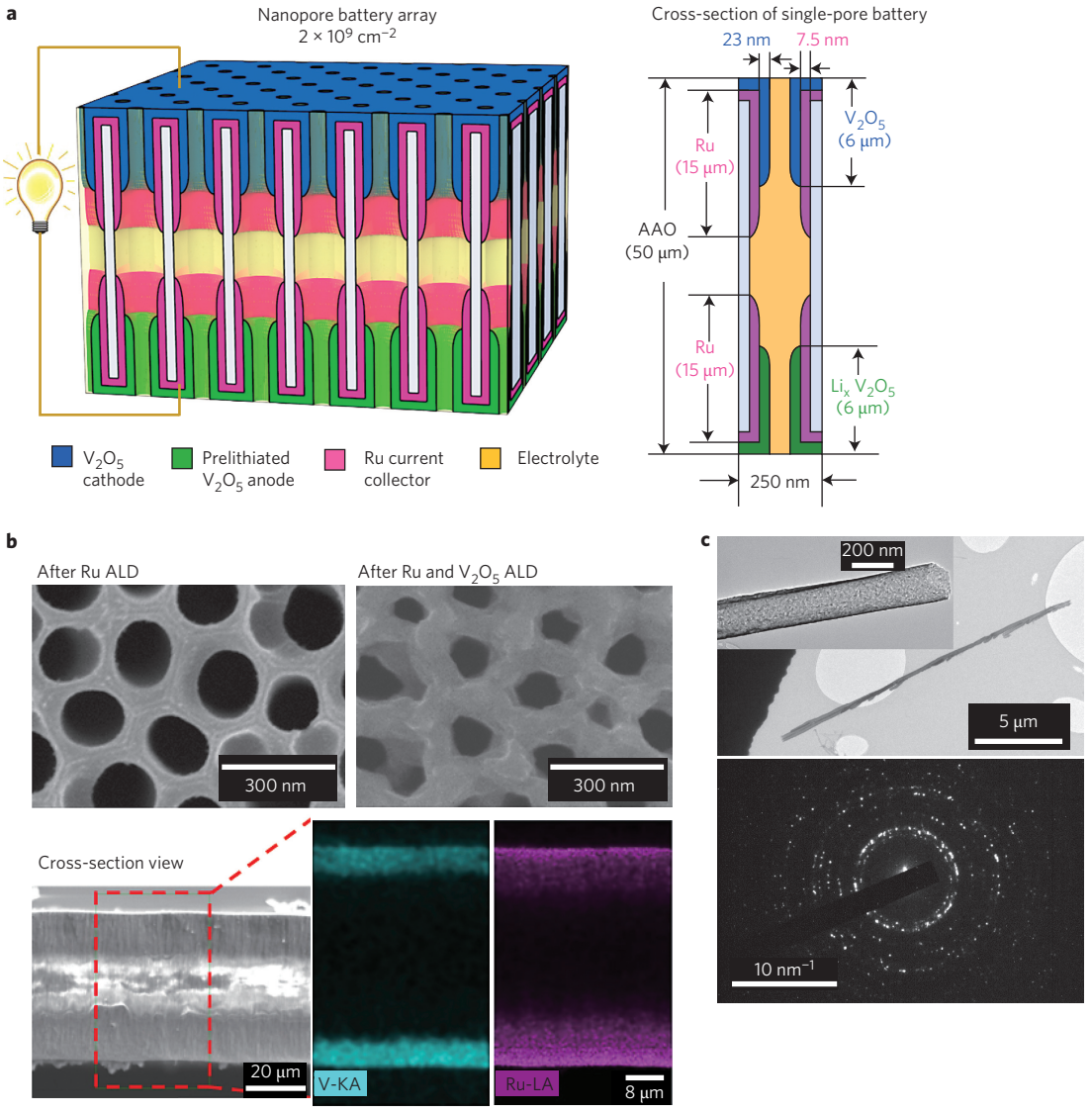

Figure 1 | Nanopore battery geometry. a, Schematic of parallel nanopore battery array and cross-section of a single-pore battery. **b**, Upper panels: SEM images of device (top view), showing AAO pores remaining open after Ru, and Ru and V_2O_5 ALD. Lower panels: EDS mapping of device cross-section, demonstrating that Ru grows ~15 μm and V_2O_5 grows 6 μm into nanopores, in a symmetrical manner. **c**, Upper panel: TEM image of a released Ru nanotube (300 ALD cycles) prepared from an AAO template (~15 μm long and 170 nm in diameter). Inset: Magnified image of Ru nanotube. Lower panel: Selected area electron diffraction (SAED) image, indicating the clear crystallinity of the Ru.

Here, we report a full battery comprising an array of nanotubular electrodes and a liquid electrolyte confined within AAO nanopores, connected in parallel to form an all-in-one device. The nanoelectrodes are composed of Ru-nanotube current collectors with V_2O_5 storage material on top to form a symmetric cell, where the anode and cathode are separated by an electrolyte region. When filled with a conventional liquid electrolyte, our nanopore-array battery achieves the full theoretical capacity expected for the V_2O_5 storage material (147 mAh g^{-1} with one Li ion per V_2O_5 insertion) and power levels about tenfold higher than those previously reported for aligned nanostructured batteries[3,5]. The capacity retention at high power is 95% at 5 C and 46% at 150 C (24 s charge–discharge cycle), relative to 1 C values. At the 5 C rate, 81% of capacity is retained after 1,000 cycles.

Nanopore battery design

We designed a single nanotube structure that embeds all the components of an electrochemical storage device (illustrated schematically in Fig. 1a) within the pores of a nanoscale template. Integrated current collectors (Ru metal) and active storage material (crystalline α-V_2O_5) were conformally coated at two ends of AAO nanotube arrays by atomic layer deposition (ALD). V_2O_5 at one end was prelithiated to serve as the anode, while pristine V_2O_5 at the other end served as the cathode. The detailed fabrication procedure is described in the Methods. After filling 1 M $LiPF_6$ in ethylene carbonate (EC): diethyl carbonate (DEC) (1:1 by volume) electrolyte into the AAO nanopores, we achieved parallel nanobattery arrays with an areal density of 2×10^9 cm^{-2}. Figure 1a illustrates the cross-section of a single cell with 250 nm outer diameter and 50 μm length, defined by the AAO geometry. A 7.5-nm-thick Ru layer (150 ALD cycles of 0.5 Å/cycle) resulted in a conductivity of 1.5×10^4 S cm^{-1} (ref. 18), enabling fast electron transport inside each electrode. Each V_2O_5 nanotube had a wall thickness of 23 nm and length of 6 μm, determined by ALD cycles (700 cycles of 0.33 Å/cycle)[19] and scanning electron microscope (SEM) with energy-dispersive X-ray spectroscopy (EDX) (Fig. 1b). This coaxial nanotube array architecture overcomes the challenge of fabricating full cells on a single substrate, using controlled-conformality ALD

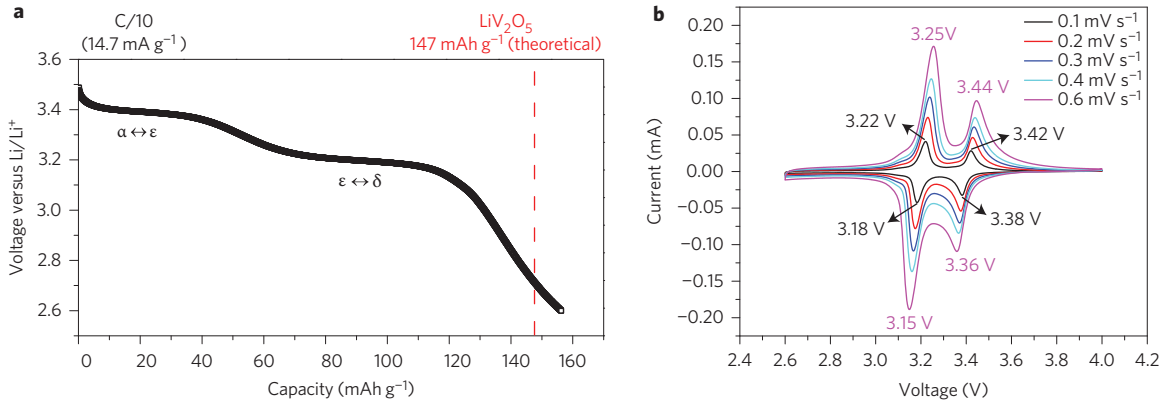

Figure 2 | Electrochemical charge–discharge of a V_2O_5/Ru nanotube half-cell device. a, Galvanostatic Li ion insertion at C/10 rate with one Li ion insertion at the first cycle. Plateaux at 3.4 V and 3.2 V correspond to phase transformation from α-V_2O_5 to ε-V_2O_5 ($V_2O_5 + 0.5Li^+ + 0.5e^- \leftrightarrow Li_{0.5}V_2O_5$) and ε-$V_2O_5$ to δ-V_2O_5 ($Li_{0.5}V_2O_5 + 0.5Li^+ + 0.5e^- \leftrightarrow LiV_2O_5$), respectively[20]. **b**, CV of V_2O_5/Ru nanotube cathode at different scan rates implies a reversible Li^+ insertion reaction. A fraction of V^{5+} ions are reduced to V^{4+} ions at the first reduction peak (~3.4 V) while the remaining V^{5+} ions are reduced to V^{4+} at the second peak (~3.2 V)[20]. The reverse reactions lead to the two corresponding oxidation peaks in the reverse scan.

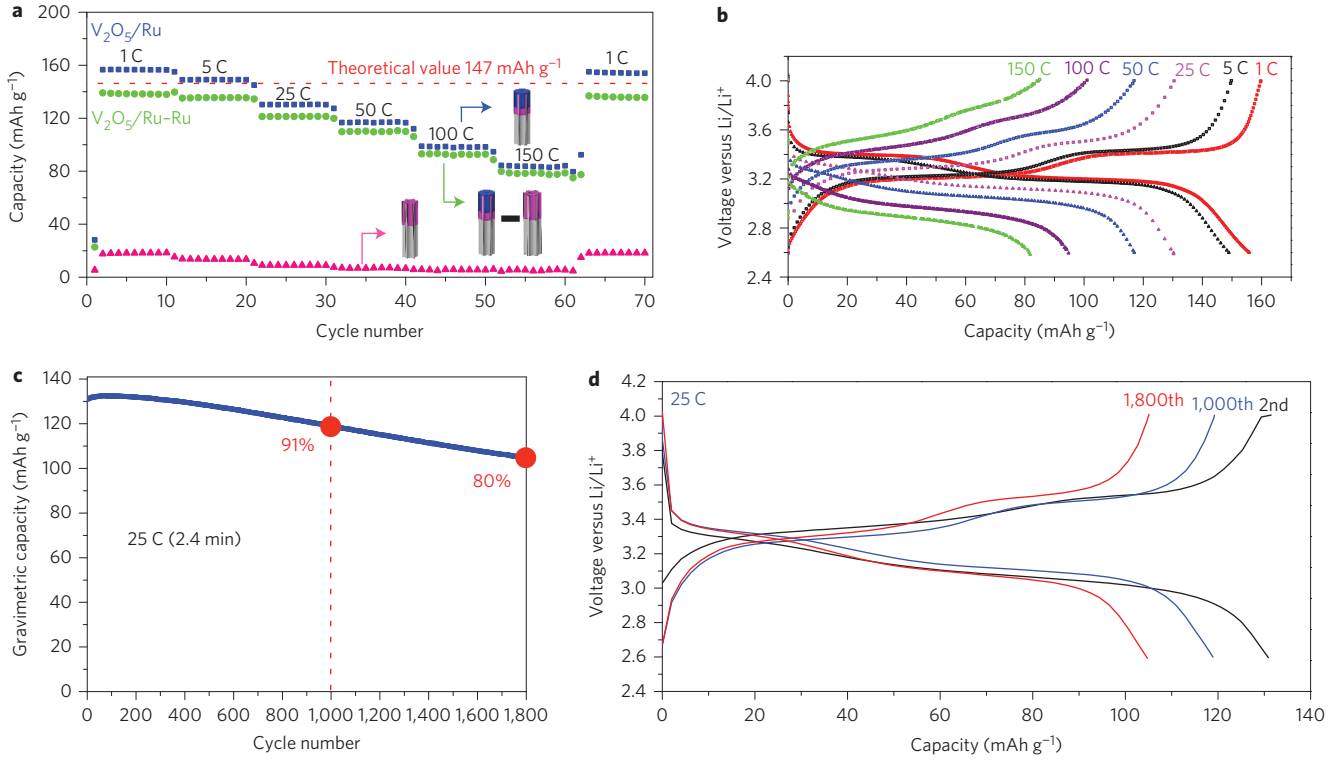

Figure 3 | Electrochemical charge–discharge of a half-cell device at high-rate cycle life. a, Rate performance of V_2O_5/Ru-nanotube battery (blue), O_3-treated Ru current collector (pink) and pure contribution of V_2O_5 (green). Inset: Cartoons represent the configuration of each case. **b**, Galvanostatic charge–discharge cycling curves of V_2O_5/Ru-nanotube cathode at various C rates. **c**, V_2O_5/Ru-nanotube cathode has 91% of the original capacity after 1,000 cycles and 80% after 1,800 cycles when cycled at 25 C. **d**, Charge–discharge curves at the second, 1,000th and 1,800th cycles.

at the ends of the AAO nanopores. The approach also takes advantage of the anode–cathode electrical isolation provided by the long AAO nanopores to achieve precise control over cell geometries and anode–cathode distances. With anode and cathode precisely aligned in each single cell, this design avoids tortuosity and maximizes control over disparate length scales, providing optimum conditions for a high-power device.

Half-cell electrochemical characterization

Half cells were tested to investigate the electrochemical properties of the V_2O_5/Ru nanotube electrodes, demonstrating that their energy storage capacity arises mainly from the active V_2O_5, with the Ru-nanotube current collectors providing high electrical conductivity.

We observed a high specific capacity of 157 mAh g^{-1} for one Li ion insertion (Fig. 2a), as indicated by phase-changing plateaux at 3.4 V and 3.2 V (versus Li/Li^+)[20]. Cyclic voltammograms (CVs) of V_2O_5 in the potential range 2.6 – 4 V (versus Li/Li^+) (Fig. 2b) further demonstrate the Li ion insertion mechanism, which occurs in two sequential stages denoted by two sets of well-resolved peaks. The two redox peaks look symmetric, and all the peak potentials shift less than 30 mV in this scan range, which implies a quite reversible Li insertion reaction.

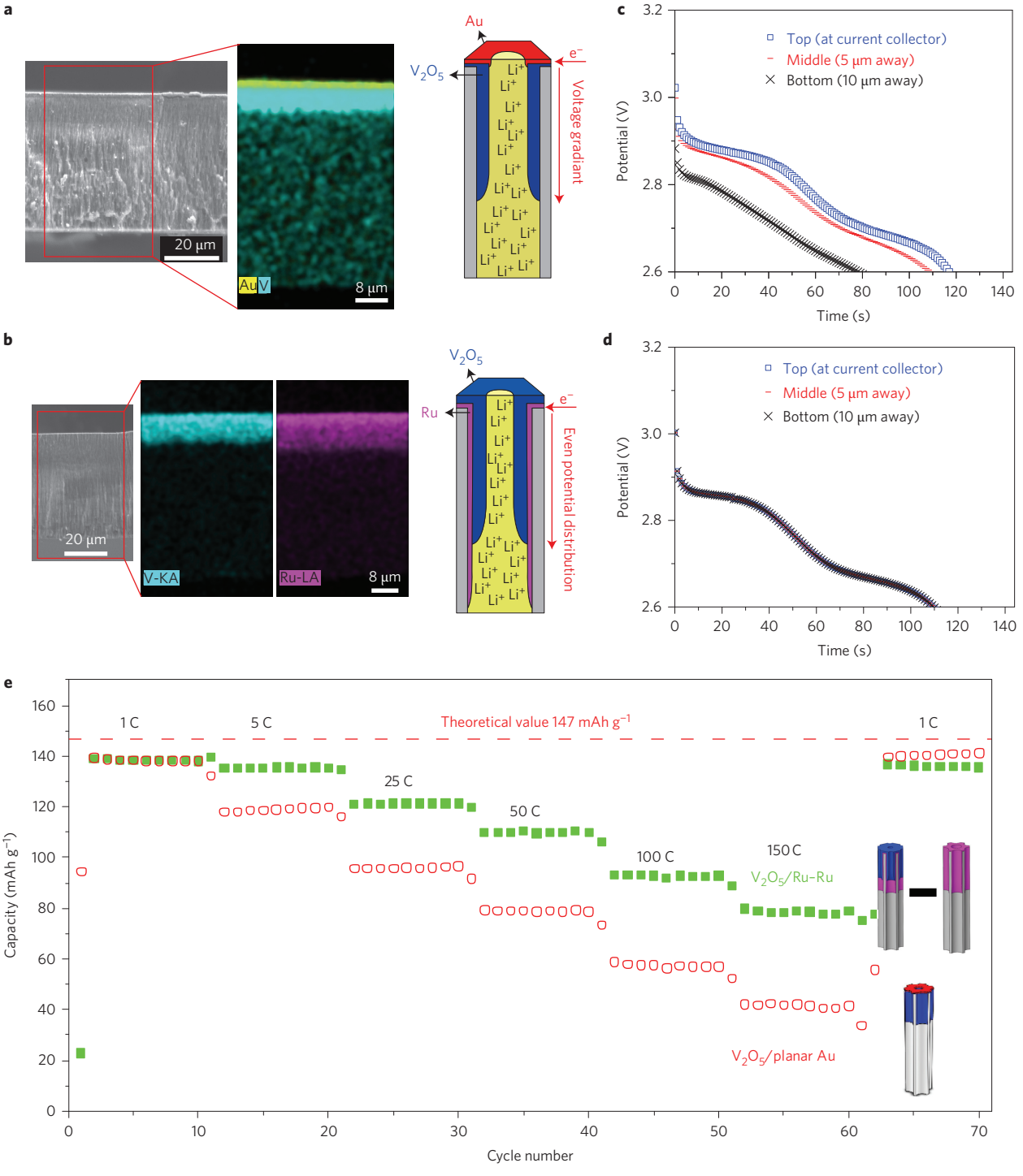

Figure 4 | Rate performance of V_2O_5 nanotube half cell with planar Au versus Ru-nanotube current collectors. a,**b**, SEM EDS mappings and schematic diagrams of cathode cross-section with Au planar current collector and Ru-nanotube current collector. **c**,**d**, COMSOL simulations of potential evolution at three different points (at current collector, 5 μm away and 10 μm away) along a V_2O_5 nanotube discharged at 25 C with planar and nanotube current collectors, respectively. **e**, Rate performance up to 150 C of V_2O_5/Ru-nanotube cathode (with Ru capacity portion subtracted, green) and V_2O_5/planar Au (red). Cartoons represent the configuration of each case.

The V_2O_5 cathode with integrated Ru-nanotube current collector displays high capacity at high charge–discharge rates. Its specific capacity has been measured to be 157 mAh g^{-1} at 1 C, over 147 mAh g^{-1} at 5 C and 83 mAh g^{-1} (53% of its original capacity at the 1 C rate) at 150 C (24 s charging time) (Fig. 3a). Interestingly, excess capacity somewhat beyond the theoretical level (147 mAh g^{-1} for one Li insertion reaction per V_2O_5 formula unit) was observed at the 1 C rate and lower. The excess capacity could be associated with the electrical double-layer capacity due to the large surface area[21] and/or the additional redox activity of possible RuO_2 formed on the Ru surface as a result of O_3 exposure during the V_2O_5 ALD process. Experiments using Ru/surface RuO_2 electrodes to simulate such redox activity showed such contributions to be small (Fig. 3a, Supplementary Section 1 and Supplementary Fig. 1).

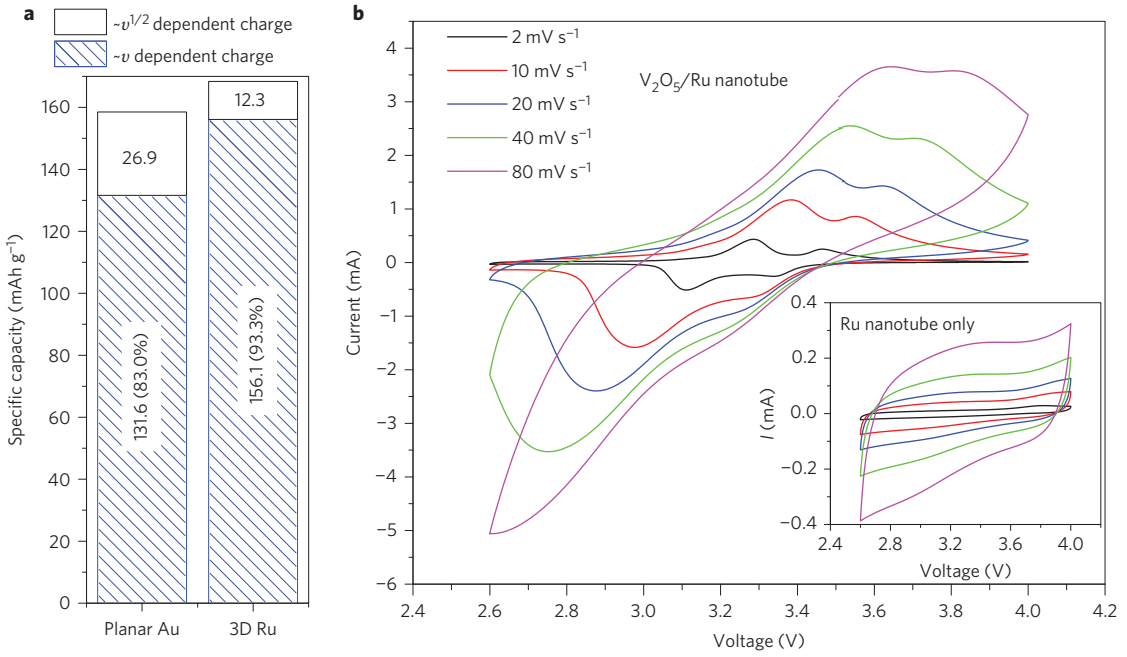

Figure 5 | Deconvolution of charge contributions from CVs. a, Trasatti's method of deconvoluting charge storage contributions as a function of scan rates indicates that the Ru-nanotube collectors facilitate a fast electrochemical reaction, resulting in both higher overall capacity and a higher contribution from the v-dependent charge, which includes the contribution of the electrical double layer and all fast Faradaic reactions, which are not diffusion-limited. **b**, CVs of V_2O_5/Ru nanotubes showing characteristic oxidation and reduction reaction peaks with scan rates up to 80 mV s^{-1}. Inset: CVs of Ru nanotubes cycled at the same scan rate, clearly showing only double-layer charging, without any of the characteristic redox peaks.

The plateaux in galvanostatic charge–discharge cycling curves (Fig. 3b) clearly show the existence of Faradaic Li ion insertion processes from 1 C to 150 C rates. This coaxial V_2O_5/Ru nanotube structure also demonstrates an exceptional charge–discharge cycle life. When cycling at 25 C, the V_2O_5/Ru coaxial nanotube cathode has 91% of its original capacity after 1,000 cycles and 80% after 1,800 cycles (Fig. 3c). The charge–discharge curves at the second, 1,000th and 1,800th cycles plotted in Fig. 3d show steady phase transition plateau positions during cycling, indicating stable voltage output during the long reversible battery cycling life. The cyclability and capacity retention at a high rate in our all-in-one array battery compare favourably with other reported cathode configurations using nanostructured V_2O_5 (refs 22, 23).

Maximizing power density in nanostructured electrodes

To further investigate the contribution of the Ru-nanotube current collectors in the facile transfer of electrons from Ru to the V_2O_5 layer in the present coaxial nanotube structure, a current collector with planar structure was tested as a control. We designed the control device to have 6-μm-deep V_2O_5 but only sputtered Au as the planar current collector (Fig. 4a) (instead of nanotubular Ru). In this structure, the electron transport path length from Au through the V_2O_5 is nearly 6 μm (to reach the bottom end of the V_2O_5 nanotube), up to 260 times longer than the electron path length (23 nm) in the V_2O_5/Ru coaxial nanotube structure in Fig. 4b. In this case a potential gradient can develop along the V_2O_5 nanotube during the charge–discharge cycle, leading to an inhomogeneous current distribution along the length of the V_2O_5 nanotube that will be especially detrimental at high cycling rates. This hypothesis was confirmed by our COMSOL simulations (Fig. 4c,d), which monitored the potential evolution at three different points along a V_2O_5 nanotube discharged at 25 C. The simulations revealed that the further from the current collector, the faster the voltage of the V_2O_5 drops in the planar current collector configuration. This inhomogeneous discharging profile results in a lower capacity than a V_2O_5 nanotube with integrated Ru-nanotube current collector, which has a uniform potential profile along the V_2O_5 nanotube at 25 C. For a discussion of the simulation details see Supplementary Section 2 and Supplementary Figs 2 and 3.

The much higher capacity of the V_2O_5/Ru-nanotube configuration than the V_2O_5/planar Au arrangement at high rates (Fig. 4e) underscores the importance of integrated current collector components in nanostructured electrodes for electron communication to and from the ion storage material. Furthermore, the high surface area and thin nature of the nanotube structure improves ion access and transport to/from the electrolyte to fully utilize the electrode material. Although the distinct peaks in the CVs and plateaux in the galvanostatic discharge curves clearly show the characteristics of a Li insertion reaction, the high capacity remaining at high rates suggests the need for further investigation into the kinetics of the devices. Trasatti's method[24] was used to distinguish the contributions from fast, surface-dominant (proportional to scan rate v) and slower, diffusion insertion-dominant reactions (proportional to $v^{1/2}$). A detailed discussion can be found in Supplementary Section 3 and Supplementary Figs 4–8.

The v-dependent surface-dominant reaction charge for the V_2O_5/Ru-nanotube half cell is predicted to be 93.3% of the total charge, which is 10% more than that of the V_2O_5/planar Au counterpart (83.0%) (Fig. 5a). Very importantly, the CVs of V_2O_5/Ru-nanotube electrodes imply that most of these reaction charges are due to a Faradaic reaction process, as they show characteristic oxidation and reduction reaction peaks at scan rates up to 80 mV s^{-1} and much higher current values than the Ru-nanotube control sample without V_2O_5, which shows only electrical double-layer capacity (Fig. 5b). This suggests that most of the Li ion-inserting Faradaic reactions of V_2O_5 nanotubes are taking place quickly enough to be indistinguishable from fast surface-dominant reactions. In conclusion, these structures have an active material thickness that is optimized to maximize the power density by utilizing the

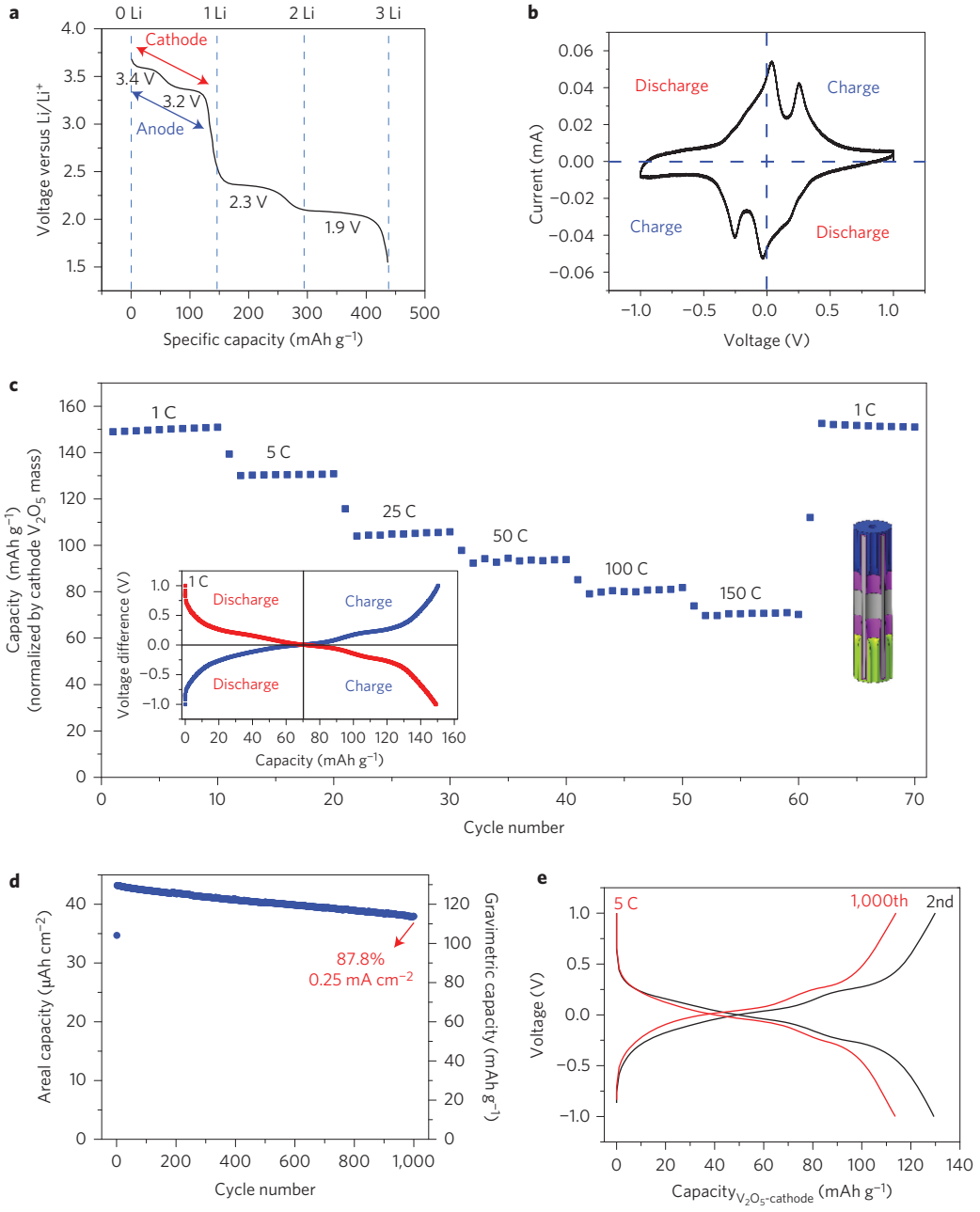

Figure 6 | Symmetrically cycled full cell with voltage window from −1 V to 1 V. a, Schematic diagram of cathode and anode voltage range. They are both in one Li ion insertion regime (4.0 V to 2.6 V). Phase transition plateau voltages are marked under the discharge curve. This V_2O_5 discharging curve is modified with permission from ref. 22, © 2011 The Royal Society of Chemistry. **b**, CV at 0.5 mV s^{-1} scan rate. **c**, Rate performance (capacity normalized by cathode V_2O_5 mass). Inset: Charge and discharge curves at 1 C. **d**, Long cycle life with high current density. **e**, Charge and discharge curves at the second and 1,000th cycles.

available material so quickly that the kinetics of this insertion reaction are nearly indistinguishable from fast double-layer charging behaviour. In an important sense, this realizes the value nanostructuring offers for achieving high power from high-energy-density storage materials.

Demonstration of a symmetric full-cell device

A full-cell device can demonstrate the potential of this architecture to translate half-cell performance into usable, complete devices that do not sacrifice the high-rate performance characteristics measured in half cells. Figure 6 summarizes the electrochemical performance of a symmetrical full-cell device, which has 106 μg V_2O_5 as the cathode and 131 μg V_2O_5 as the anode. The anode V_2O_5 was prelithiated at 1 C current to 2.6 V versus Li/Li^+ with one Li ion insertion. The cell was then cycled within a symmetric voltage window between −1 V and 1 V. During the cycling process, the cathode and anode switched between LiV_2O_5 and V_2O_5 in turn (Fig. 6a).

Figure 6b presents a CV of the full-cell device at a scan rate of 0.5 mV s^{-1}, with two reduction peaks at −0.03 and −0.25 V and their corresponding oxidation peaks at 0.25 V and 0.04 V in the reverse scan, respectively. The differences between the reduction and oxidation peaks are therefore 0.28 V and 0.29 V for the two characteristic reaction peaks. Although naturally slightly larger than the half-cell peak separation (0.2 V), the full cell still shows good reversibility. The C rate and specific capacity were normalized by the weight of the V_2O_5 cathode. The nanopore battery full cell

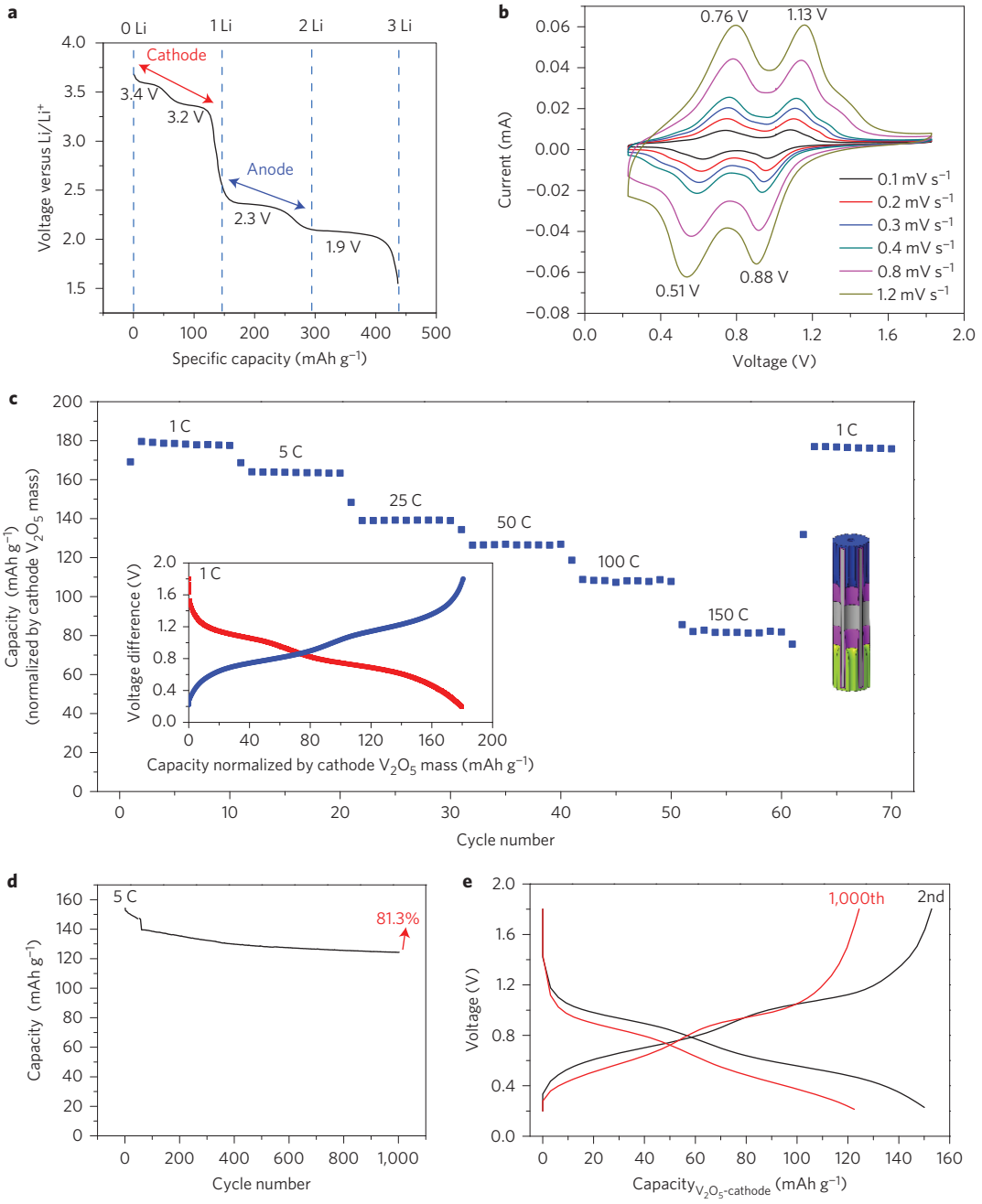

Figure 7 | Asymmetrical cycling between 0.2 V and 1.8 V. a, Schematic of cathode and anode voltage range. The cathode is cycled in one Li ion insertion regime (4.0–2.6 V), while the anode is cycled in two Li ion insertion regimes (2.6–2.1 V), providing higher output potential than the symmetrical cell in Fig. 6. Phase transition plateau voltages are marked under the discharge curve. This V_2O_5 discharging curve is modified with permission from ref. 22. © 2011 The Royal Society of Chemistry. **b**, CVs at different scan rates. **c**, Rate performance (capacity normalized by cathode V_2O_5 mass). Inset: Charge and discharge curves at 1 C. **d**, Cycling performance at 5 C. **e**, Charge and discharge curves at the second and 1,000th cycles.

has a capacity of 150 mAh g^{-1} at 1 C and 70 mAh g^{-1} at 150 C (Fig. 6c), which is consistent with the half-cell performance in terms of capacity retained at high rate. Interestingly, this seems to indicate that the confined electrolyte space is not a severely limiting factor in these devices. Furthermore, 87.8% of the original capacity remains after 1,000 cycles at a 5 C rate with a current density of 0.26 mA cm^{-2} (Fig. 6d). Compared to a nanowire array full-battery device inside AAO as reported previously[5], this nanopore battery has triple the capacity, with hundreds of times longer cycle life, even at a much higher power density (eight times the current density). We attribute the superior lifetime to the conformal coaxial tubular structure enabled by ALD, which reduces inhomogeneous charging at the irregular sharp edges of the electrodes[25–27] and provides reliable mechanical strength during cycling[28]. Additionally, the good crystallinity of V_2O_5 increases reversibility during lithiation and delithiation[19].

Scaling up energy and power density

Increasing the cell voltage is a possible method to improve the energy and power density. A full-cell device with a voltage window from 0.2 V to 1.8 V was demonstrated by cycling the cathode between V_2O_5 and LiV_2O_5 and the anode between $Li_2V_2O_5$ and LiV_2O_5 (Fig. 7a). With this arrangement, mass loading at the cathode side was half that at the anode side to

compensate for a possibly faster capacity fade rate of the anode than of the cathode. The specific capacity, normalized by the mass of the anode, is comparable to that of the half cell, with 178 mAh g^{-1} at the 1 C rate and 82 mAh g^{-1} at the 150 C rate (Fig. 7c). The CV curve at a scan rate of 1.2 mV s^{-1} (Fig. 7b) displays two characteristic reduction peaks for phase transitions during one Li ion insertion, at 0.88 V and 0.51 V, with the corresponding oxidation peaks at 1.13 V and 0.76 V. Redox peak and oxidation peak separations are both 0.37 V, but this full cell with voltage window from 0.2 V to 1.8 V still displays excellent reversibility and cycling performance with 81.3% capacity remaining after 1,000 cycles (Fig. 7d).

Based on the electrochemical performance of the full-cell device, we predicted high volumetric energy and power density with optimized AAO geometry and storage material mass loading. The AAO template used in this study has a porosity of ~32%, but can be increased (for example, by pore widening) up to 55%. Accordingly, cathode mass loading could be increased by a factor of 4.8 (Supplementary Table 3). In addition, if the battery output potential is doubled by replacing the anode side with other low-voltage materials, the total energy and power density could potentially be increased to 9.6 times that of the present design, reaching 3.8 μWh $μm^{-1}$ cm^{-2} and 1,012 μW $μm^{-1}$ cm^{-2}.

Conclusions

We have reported an all-in-one nanopore array battery that exemplifies the advantages of nanostructured electrodes, without some of the disadvantages related to the extreme confinement of the electrolyte solution. Our array battery, in both half- and full-cell configurations, shows excellent capacity retention (~50% at the 150 C rate, relative to 1 C), providing ~80 mAh g^{-1} at 150 C (24 s charge–discharge time) with more than 80% of initial capacity retained after 1,000 cycles at 5 to 25 C. These performances are a direct consequence of the nanotubular electrode design, in which a thin storage layer (V_2O_5) and an integrated current-collecting layer (Ru) deposited through ALD facilitate fast ion and electron transport, respectively. We suggest that nanotubular electrodes may expand inward upon lithiation, forming uniform structures within the nanopores and across the arrays of nanopore batteries derived from the self-assembled AAO template. By extending the design to larger dimensions (for example, through AAO pore widening, thicker storage layers and so on, as detailed in Supplementary Table 3) and full-cell output voltage, we anticipate the possibility of considerable improvement in power and energy density. Our results are also important from a fundamental point of view, in particular to elucidate ion transport in highly confined electrolyte environments, a key factor that is bound to affect any nanostructure-based energy storage approach. In our case, the theoretical capacity of the active storage material is achieved at high power, yet our analysis (by the Trasatti method) shows that the specific capacity scales linearly with scan rates, as expected for charged surfaces or electrical double layers. This demonstrates that properly scaled nanostructures can utilize the full theoretical capacity of the charge storage material while their ion insertion processes occur at high power, much like what happens in a double-layer capacitor, indeed blurring the traditional distinction between surface effects and ion insertion. Although the effect of electrolyte confinement was not the primary focus of this study, there are a variety of geometrical modifications that can be applied to our design to help characterize ion transport limits in nanostructured energy storage and offer guidelines for optimized nanoelectrode geometries.

Methods

Symmetric AAO templates (thickness, 50 μm; pore diameter, 150 nm; pore period, 340 nm) were purchased from Synkera. We chose a Ru ALD process that is well established in our laboratory for fabricating current collectors, although a variety of other inexpensive conducting materials (including titanium nitride, tungsten[29,30] and nickel[31]) are also achievable via ALD. Ru ALD using bis(2,6,6-trimethyl-cyclohexadienyl)ruthenium ($Ru(C_9H_{13})_2$, 'Cyprus') and O_2 was carried out in a home-built viscous flow reactor furnace at 300 °C. The deposition rate was 0.5 Å/cycle, yielding a 7.5 nm film for a 150-cycle process with a conductivity of $\sim 1.5 \times 10^4$ S cm^{-1}. The detailed process parameters and Ru thin-film conductivity have been described in our previous papers[18,32]. During the Ru ALD process for a full cell, the AAO templates were pressed between two 1/2-inch nickel VCR face seal fitting gaskets with 0.44-inch inner diameter (0.95 cm^2 opening; Swagelok), the edges of which were then wrapped in aluminium foil and finally fixed using metal binder clips. The VCR gaskets served as contact masks to prevent Ru growth at the rim of the AAO, which might cause shorting between the anode and cathode sides. The 5 s pulse time was chosen for the Cyprus to limit the Ru deposition depth to 15 μm into the AAO pores, leaving 20 μm of bare AAO in the middle to act as a separator. Subsequently, crystalline V_2O_5 was deposited by ALD using vanadyl triisopropoxide ($VO(OC_3H_7)_3$, VTOP) and ozone at 170 °C in a BENEQ TFS 500 reactor. Home-made contact masks with a 6-mm-diameter opening controlled V_2O_5 growth into one side of the Ru-coated AAO pores with a deposition rate of 0.33 Å/cycle to form nanotubes with a wall thickness of 23 nm. The V_2O_5 grew 6 μm into the pores with a 1 s VTOP pulse time. The same procedure was then repeated to grow V_2O_5 symmetrically at the other end of the Ru-coated AAO. The area of a full-cell device is defined by the open area of the contact mask (0.28 cm^2) and was further measured by counting the pixels of the V_2O_5-covered area (0.32 cm^2), as shown in Supplementary Table 1. Commercially available templates can be purchased with areas as large as 1,200 cm^2 (http://www.synkerainc.com), suggesting that there is room for scaling up this design (Supplementary Fig. 11 shows an intact AAO electrode after reopening a coin cell). Subsequently, one side of the V_2O_5 was electrochemically lithiated by discharging at a 1 C rate to different voltages (2.6 V and 2.1 V versus Li metal). This prelithiated V_2O_5 was used as the anode of the full-cell batteries. For half-cell fabrication, a similar masking method was used with a VCR gasket sealing one side of the AAO against a solid plate during both Ru and V_2O_5 ALD process, resulting in an area of 0.95 cm^2. The mass of V_2O_5 was measured using a microbalance before and after V_2O_5 ALD.

The O_3-treated Ru nanotubes in the AAO template were prepared by ALD, coating Ru to the AAO template, then treating with O_3 while omitting the vanadium precursor (VTOP) during the V_2O_5 ALD process. We prepared the control device with V_2O_5 nanotubes but planar Au as the current collector by ALD-depositing V_2O_5 into AAO pores, and then sputtering (using a Denton Vacuum Desktop III) a thin layer of Au on top to provide lateral conductivity comparable to a Ru-integrated current collector, without blocking the pore openings (Supplementary Fig. 13). The performance of this planar current collector device was compared with a three-dimensional integrated current collector device by galvanostatic cycling at the same C rate. Meanwhile, finite-element simulation was performed using COMSOL Multiphysics software to simulate the discharge capacity of the V_2O_5 nanopore cathode with these two different current collector geometries.

Material characterization was conducted using a Hitachi SU-70 analytical SEM with EDX capability. To verify the conformality of Ru, the AAO template was dissolved in 0.3 M NaOH and Ru nanotubes were collected on a copper grid for transmission electron microscopy (TEM) analysis using a JEOL 2100F. An Arbin BT-2000 multichannel battery test station was used for galvanostatic charging and discharging at various rates and to collect the CV data in Fig. 6b. Other CV data were collected from a Bio-logic VSP using EC-lab software. The electrode mass was measured using a Sartorius ME5 microbalance.

Received 9 April 2014; accepted 24 September 2014; published online 10 November 2014

References

1. Rhodes, C., Long, J., Pettigrew, K., Stroud, R. & Rolison, D. Architectural integration of the components necessary for electrical energy storage on the nanoscale and in 3D. *Nanoscale* **3,** 1731–1740 (2011).
2. Long, J., Dunn, B., Rolison, D. & White, H. Three-dimensional battery architectures. *Chem. Rev.* **104,** 4463–4492 (2004).
3. Sun, K. *et al.* 3D printing of interdigitated Li-ion microbattery architectures. *Adv. Mater.* 4539–4543 (2013).
4. Pikul, J. H., Zhang, H. G., Cho, J., Braun, P. V. & King, W. P. High-power lithium ion microbatteries from interdigitated three-dimensional bicontinuous nanoporous electrodes. *Nature Commun.* **4,** 1732 (2013).
5. Gowda, S. R., Reddy, A. L. L. M., Zhan, X. & Ajayan, P. M. Building energy storage device on a single nanowire. *Nano Lett.* **11,** 3329–3333 (2011).
6. Banerjee, P., Perez, I., Henn-Lecordier, L., Lee, S. B. & Rubloff, G. W. Nanotubular metal–insulator–metal capacitor arrays for energy storage. *Nature Nanotech.* **4,** 292–296 (2009).
7. Haspert, L. C., Lee, S. B. & Rubloff, G. W. Nano-engineering strategies for metal–insulator–metal electrostatic nanocapacitors. *ACS Nano* **6,** 3528–3536 (2012).
8. Haspert, L. C., Gillette, E., Lee, S. B. & Rubloff, G. W. Perspective: hybrid systems combining electrostatic and electrochemical nanostructures for ultrahigh power energy storage. *Energy Environ. Sci.* **6,** 2578–2590 (2013).
9. Ruzmetov, D. *et al.* Electrolyte stability determines scaling limits for solid-state 3D Li ion batteries. *Nano Lett.* **12,** 505–511 (2011).

10. Vahur, Z. & Daniel, B. Modelling polymer electrolytes for 3D-microbatteries using finite element analysis. *Electrochim. Acta* **57,** 237–243 (2011).
11. Arthur, T. S. *et al.* Three-dimensional electrodes and battery architectures. *MRS Bull.* **36,** 523–531 (2011).
12. Gerasopoulos, K. *et al.* Hierarchical three-dimensional microbattery electrodes combining bottom-up self-assembly and top-down micromachining. *ACS Nano* **6,** 6422–6432 (2012).
13. Gnerlich, M. *et al.* Solid flexible electrochemical supercapacitor using Tobacco mosaic virus nanostructures and ALD ruthenium oxide. *J. Micromech. Microeng.* **23,** 114014 (2013).
14. White, R. & White, H. Electrochemistry in nanometer-wide electrochemical cells. *Langmuir* **24,** 2850–2855 (2008).
15. Matt, K. P., Revati, K., Henry, S. W. & Gregory, A. V. A computationally efficient treatment of polarizable electrochemical cells held at a constant potential. *J. Chem. Phys. C* **116,** 4903–4912 (2012).
16. Ryan, W. H., Henry, S. W., Bruce, D. & Debra, R. R. 3-D microbatteries. *Electrochem Commun.* **5,** 120–123 (2003).
17. US Department of Energy Basic Energy Sciences Advisory Committee Mesoscale Science Committee W. *From Quanta to the Continuum: Opportunities for Mesoscale Science* (Government Printing Office, 2012).
18. Gregorczyk, K., Banerjee, P. & Rubloff, G. W. Conduction in ultrathin ruthenium electrodes prepared by atomic layer deposition. *Mater. Lett.* **73,** 43–46 (2012).
19. Chen, X. *et al.* Ozone-based atomic layer deposition of crystalline V_2O_5 films for high performance electrochemical energy storage. *Chem. Mater.* **24,** 1255–1261 (2012).
20. Lu, Z. *et al.* Basic electroanalytical characterization of lithium insertion into thin, well-crystallized V_2O_5 films. *J. Electroanal. Chem.* **491,** 211–221 (2000).
21. Zhou, C. F., Kumar, S., Doyle, C. D. & Tour, J. M. Functionalized single wall carbon nanotubes treated with pyrrole for electrochemical supercapacitor membranes. *Chem. Mater.* **17,** 1997–2002 (2005).
22. Wang, S. *et al.* Porous monodisperse V_2O_5 microspheres as cathode materials for lithium-ion batteries. *J. Mater. Chem.* **21,** 6365–6369 (2011).
23. Liu, Y. *et al.* V_2O_5 nano-electrodes with high power and energy densities for thin film Li-ion batteries. *Adv. Energy Mater.* **1,** 194–202 (2011).
24. Ardizzone, S., Fregonara, G. & Trasatti, S. 'Inner' and 'outer' active surface of RuO_2 electrodes. *Electrochim. Acta* **35,** 263–267 (1990).
25. Harris, S. J., Timmons, A., Baker, D. R. & Monroe, C. Direct *in situ* measurements of Li transport in Li-ion battery negative electrodes. *Chem. Phys. Lett.* **485,** 265–274 (2010).
26. Harris, S. J. & Lu, P. Effects of inhomogeneities—nanoscale to mesoscale—on the durability of Li-ion batteries. *J. Phys. Chem. C* **117,** 6481–6492 (2013).
27. Cleveland, E. R., Banerjee, P., Perez, I., Lee, S. B. & Rubloff, G. W. Profile evolution for conformal atomic layer deposition over nanotopography. *ACS Nano* **4,** 4637–4644 (2010).
28. Karki, K. *et al.* Hoop-strong nanotubes for battery electrodes. *ACS Nano* **7,** 8295–8302 (2013).
29. Lei, W. *et al.* Real-time observation and optimization of tungsten atomic layer deposition process cycle. *J. Vac. Sci. Technol. B* **24,** 780–789 (2006).
30. Grubbs, R. K., Steinmetz, N. J. & George, S. M. Gas phase reaction products during tungsten atomic layer deposition using WF_6 and Si_2H_6. *J. Vac. Sci. Technol. B* **22,** 1811–1821 (2004).
31. Kim, W-H. *et al.* Atomic layer deposition of Ni thin films and application to area-selective deposition. *J. Electrochem. Soc.* **158,** D1–D5 (2011).
32. Gregorczyk, K., Henn-Lecordier, L., Gatineau, J., Dussarrat, C. & Rubloff, G. Atomic layer deposition of ruthenium using the novel precursor bis(2,6,6-trimethyl-cyclohexadienyl)ruthenium. *Chem. Mater.* **23,** 2650–2656 (2011).

Acknowledgements

This work was supported by Nanostructures for Electrical Energy Storage (NEES), an Energy Frontier Research Center funded by the US Department of Energy, Office of Science, Office of Basic Energy Sciences (award no. DESC0001160). The authors acknowledge support from the Maryland NanoCenter and the NispLab, and thank C. Wang for providing electrolyte, M. Noked, Y. Xu and C. Sun for discussions regarding electrochemistry and J. Provine for valuable suggestions for noble-metal ALD.

Author contributions

C.L., X.C., S.B.L. and G.W.R. conceived and designed the experiments. C.L. and X.C. performed the half-cell experiments. C.L. performed the full-cell experiment. E.I.G. conducted the COMSOL simulation. A.J.P. carried out XPS characterization. K.E.G., A.C.K. and M.A.S. contributed material fabrication tools. C.L., E.I.G., S.B.L. and G.W.R. co-wrote the paper. All authors discussed the results and commented on the manuscript.

Additional information

Supplementary information is available in the online version of the paper. Reprints and permissions information is available online at www.nature.com/reprints. Correspondence and requests for materials should be addressed to S.B.L. and G.W.R.

Competing financial interests

The authors declare no competing financial interests.